

Operando studies on $\text{NaNi}_{0.5}\text{Ti}_{0.5}\text{O}_2$ cathode for Na-ion batteries: elucidating titanium as structure stabilizer

Sebastian Maletti^{*,†}, Angelina Sarapulova[‡], Alexander Schökel[§], Daria Mikhailova^{*,†}

[†] Leibniz Institute for Solid State and Materials Research (IFW) Dresden e.V., Helmholtzstraße 20, D-01069 Dresden, Germany

[‡] Institute for Applied Materials (IAM), Karlsruhe Institute of Technology (KIT), D-76344 Eggenstein-Leopoldshafen, Germany

[§] Deutsches Elektronen-Synchrotron (DESY), Notkestraße 85, D-22607 Hamburg, Germany

KEYWORDS: Layered Nickel Titanium Oxide, Sodium-Ion Batteries, Cathode Materials, Post-Lithium Technologies, Stationary Energy Storage

ABSTRACT: O₃-type layered $\text{NaNi}_{0.5}\text{Ti}_{0.5}\text{O}_2$, which has been reported previously as a promising cathode material for Na-ion batteries, has been characterized using comprehensive operando techniques combined with electrochemical and magnetization measurements. Synchrotron diffraction revealed a reversible O₃-P₃ transformation during charge and discharge without any intermediate phases, which stands in contrast to NaNiO_2 and $\text{NaNi}_{0.5}\text{Mn}_{0.5}\text{O}_2$. X-ray absorption studies showed that the electrochemical process in the potential window of 1.5–4.2 V vs. Na^+/Na is sustained exclusively by Ni oxidation and reduction while Ti remains inactive. These findings are further supported by ex situ magnetization measurements, yielding a lower paramagnetic moment in the charged state. On the basis of these insights, we elaborate on the beneficial stabilizing effect of Ti. However, a strong C-rate dependence for $\text{NaNi}_{0.5}\text{Ti}_{0.5}\text{O}_2$ and $\text{NaNi}_{0.5}\text{Mn}_{0.5}\text{O}_2$ during cycling known from the literature points at a rather high influence of the original structure stacking and the associated Na migration paths.

INTRODUCTION

As lithium-ion batteries are reaching limits in many respects, alternative chemistries for energy storage are heavily demanded. Sodium-ion batteries represent a promising way forward for economic and ecologic reasons, as sodium is far more abundant than lithium. Although their operation principle is similar to the well-known lithium chemistry, application of sodium-ion batteries is still hampered, above all by a lack of cathode materials. Presently, layered sodium oxides are the dominating material family among investigated cathodes. Single transition metal oxides such as NaNiO_2 exhibit numerous structural transformations upon desodiation and are therefore unfavorable for battery applications. Although NaNiO_2 yields a reasonable initial discharge capacity of 147 mAh g⁻¹, a low cycling stability is observed due to a series of five plateaus between 2.0 and 4.5 V vs. Na^+/Na .¹ It has been shown that as much as seven different O₃ and P₃ phases appear during a charge-discharge cycle.² These phases differ mainly in terms of the oxygen coordination of sodium which is either octahedral (O₃) or prismatic (P₃). From a practical point of view, the multi-step potential curve is unwanted since a battery should provide a constant power output. By incorporating a second element into the transition metal layers, these

structures can be stabilized and transformations can be suppressed. Moreover, a smooth potential curve is obtained.

O₃-type $\text{NaNi}_{0.5}\text{Ti}_{0.5}\text{O}_2$ has been reported first in 2014 as a Na-ion battery cathode by Yu et al.³ The authors followed the approach of Komaba et al.⁴ who had studied a solid solution of NaNiO_2 and NaMnO_2 and found Mn^{4+} to be electrochemically inactive and responsible for a significant structure stabilization. Consequently, Ti^{4+} should have a similar effect while increasing the material's sustainability. The obtained Ti-containing material exhibited 121 mAh g⁻¹ at a 0.2C current density and an impressive cycle life with a capacity retention of 75 % after 300 cycles at 1C. The structure of the pristine material was reported as a rhombohedral $\alpha\text{-NaFeO}_2$ type. However, only the unit cell dimensions are presented. Also, the structural evolution upon cycling was not studied, which leaves many explanations for the compound's electrochemical performance unrevealed. Recently, it was reported for $\text{NaNi}_{0.5}\text{Mn}_{0.5-x}\text{Ti}_x\text{O}_2$ that Ti substitution for Mn is favorable due to increased interslab distances and suppressed phase transformations in the high voltage region.⁵

Zhou's group continued research on this material and pushed the concept further by reporting symmetric sodium-ion batteries of an O_3 material with the slightly altered composition $Na_{0.8}Ni_{0.4}Ti_{0.6}O_2$.⁶ Therein, a large potential range was investigated and redox processes were observed at 3.6/3.5 V and at 0.95/0.7 V vs. Na^+/Na . Hence, it was assumed that in a symmetric cell, sodium is drawn from the cathodic half-cell by oxidizing nickel at high potentials while in the anodic half-cell sodium is inserted and titanium is reduced at low potentials. The symmetric full cells deliver an average voltage of 3 V, a capacity of 80 mAh g^{-1} and a capacity retention of 75 % after 150 cycles. This bifunctionality of layered oxides had been already reported for P2-type $Na_xNi_{x/2}Ti_{1-x/2}O_2$,⁷⁻⁹ however all the presented symmetric cells deliver capacities significantly lower than 100 mAh g^{-1} and do not offer much space for improvement. Moreover, as shown in a recent review, O_3 phases usually deliver higher reversible capacities than their P2 counterparts and offer better practicability for full cell application.¹⁰ Therefore we focused on the properties of O_3 - $NaNi_{0.5}Ti_{0.5}O_2$ as a cathode material, which offers capacities and potentials clearly exceeding 100 mAh g^{-1} and 4 V, respectively. Also, this material has been successfully tested in full cells using hard carbon anodes already.¹¹

As recent works show, the complex processes in layered sodium oxides are hard to understand using conventional *ex situ* characterization techniques, in some cases even impossible due to the metastable nature of intermediate states.^{12,13} Hence, for a comprising understanding of the material, we combined *operando* synchrotron techniques such as X-ray diffraction (XRD) for observing structural transformations and X-ray absorption spectroscopy (XAS) in order to learn about the occurring valence changes. The insights are further supported by magnetization measurements and transferred to application by accompanying electrochemical measurements.

EXPERIMENTAL

Synthesis and Characterization. O_3 - $NaNi_{0.5}Ti_{0.5}O_2$ was prepared by solid-state reaction using stoichiometric amounts of Na_2CO_3 (Merck >99.9 %), TiO_2 (Chempur >99.5 %) and $Ni(CH_3COO)_2 \cdot 4H_2O$ (Fluka, >99.0 %). Pellets made from the reactants were placed in alumina crucibles and heated up to 930 °C for 25 h in air. After heat treatment, the samples were immediately transferred to an Argon-filled glovebox with water and oxygen content less than 1 ppm.

For phase analysis of the synthesized compounds as well as of electrochemically treated *ex situ* samples, powder X-ray diffraction was carried out using a STOE STADI P diffractometer with $Co-K_{\alpha}$ radiation ($\lambda = 1.78896 \text{ \AA}$) in transmission mode. To avoid air contact, the samples were sealed between polyimide sheets.

Electrochemical Investigations. Electrochemical tests were performed in two-electrode Swagelok-type half cells using a VMP3 potentiostat (Biologic Instruments). For Galvanostatic Cycling with Potential Limitation (GCPL), cells were charged and discharged with a current of $C/20$, where 1 C corresponds to the (de-)insertion of 1 Na per formula unit within one hour. Electrodes were prepared by pressing a mixture of the active material with Super P carbon (BASF) and PTFE (Aldrich) in an 85:10:5 weight ratio onto an aluminium current collector. Sodium anodes were home-made by rolling pieces of metallic sodium (Alfa Aesar, 99.95 %) into plates and cutting out disks. A glass fiber cloth (Whatman, GE), soaked with electrolyte, served as separator. The influence of various home-made electrolytes was investigated. Therefore $NaClO_4$ (ACS, 98.0 – 102.0 %) and $NaPF_6$ (abcr, 99.0 %) salts were dissolved in propylene carbonate (PC, BASF) or a mixture of ethylene carbonate (EC, BASF) and dimethyl carbonate (DMC, BASF).

Operando X-ray Synchrotron Diffraction. *Operando* X-ray synchrotron diffraction measurements were conducted at PETRA III, beamline P02.1 (DESY, Hamburg, Germany). An eight-fold coin cell holder, connected to a Biologic Instruments potentiostat, was applied as described in our earlier work.¹⁴ A wavelength of 0.20737(1) Å was determined by a refinement from the reflections of the LaB_6 reference material. For characterization of pristine materials, the first diffraction pattern was recorded before starting the electrochemical measurement. Subsequently, the cells were charged and discharged at a constant current. All diffraction patterns were analysed by the Rietveld method using Fullprof.¹⁵ Reflections of the Al current collector served as an internal standard during the measurements providing an independent control of the reliability of the obtained model parameters.

Operando X-ray Absorption. *Operando* X-ray absorption experiments were carried out at the beamline P65 at PETRA III extension (DESY, Hamburg, Germany) in transmission and fluorescence setup. As described for the *operando* XRD measurements, a coin cell holder, coupled with a Biologic Instruments potentiostat, was used for electrochemical cycling. For EXAFS data analysis, the measured spectrum below the pre-edge region was fitted linearly while the post-edge background contribution was fitted to a quadratic polynomial. This background $\mu_o(E)$ was subtracted from the absorption spectrum $\mu(E)$ and the resulting data were normalized according to the formula $\chi(E) = \{\mu(E) - \mu_o(E)\} / \Delta\mu_o(E)$, where $\Delta\mu_o(E)$ denotes the measured jump in absorption at the edge. The normalized spectrum was converted into k space using $k = [2m(E - E_0) / \hbar^2]^{1/2}$. By weighting $\chi(k)$ with k^3 , contributions of higher k space were amplified. The resulting $k^3\chi(k)$ was Fourier-transformed into the R space, allowing the determination of bond contributions. Least-square fits were performed using the FEFF6 code.¹⁶

SQUID Magnetometry. Magnetization measurements of pristine $\text{O}_3\text{-NaNi}_{0.5}\text{Ti}_{0.5}\text{O}_2$ and products of desodiation/sodiation were performed using a SQUID magnetometer (MPMS) from Quantum Design. The temperature dependencies of the magnetization were measured both in zero-field-cooled (ZFC) and in field-cooled (FC) mode between $T = 2$ and 330 K at 6 T. Magnetic susceptibilities in the paramagnetic region were analysed in terms of the modified Curie-Weiss law with a temperature-independent paramagnetic contribution χ_0 : $\chi = C/(T-\theta) + \chi_0$, where the Curie constant $C = N_A\mu_{\text{eff}}^2/3k_B$ yields the paramagnetic effective moment μ_{eff} .

RESULTS AND DISCUSSION

Solid State Synthesis. O_3 -type $\text{NaNi}_{0.5}\text{Ti}_{0.5}\text{O}_2$ was obtained by a simple calcination of powder agents. The obtained diffraction pattern is presented in Figure 1, corresponding structural information is presented in Table S1. As depicted, a small percentage of NiO (~7 mol-%) is present in the material. The appearance of this phase seems inevitable, despite all synthesis efforts, which is consistent with the available literature.^{3,6}

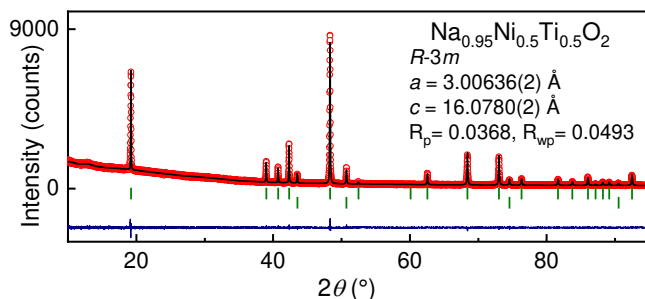


Figure 1. XRD of the as-synthesized $\text{NaNi}_{0.5}\text{Ti}_{0.5}\text{O}_2$ compound ($\lambda = 1.78896 \text{ \AA}$). Red circles represent measured intensity, the black line indicates the calculated pattern; the difference between both is shown in blue. Green bars indicate Bragg positions of $\text{NaNi}_{0.5}\text{Ti}_{0.5}\text{O}_2$ (upper row) and NiO (lower row).

Electrochemical Characterization. The material exhibits the same charge-discharge behaviour that has already been reported,³ see Figure 2. The charge half cycle starts with a flat plateau-like region closely above 3 V, followed by a more sloping region, consuming more than 150 mAh g^{-1} . The subsequent discharge profile proceeds nearly linearly until 3 V, where a short plateau follows, leading into a steeply sloping region. At the cutoff voltage of 1.5 V, a discharge capacity of 120 mAh g^{-1} is delivered, which is remarkably less than the charge capacity.

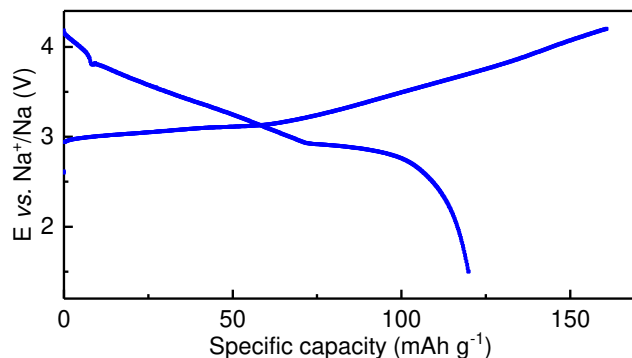


Figure 2. First charge-discharge cycle of the title compound between 4.2 V and 1.5 V vs. sodium using a NaClO_4 in EC:PC electrolyte.

Operando Evaluation of Reaction Mechanism (I): Average Crystal Structure.

In order to follow structural changes accompanying sodium extraction and insertion, we carried out *operando* synchrotron diffraction in the first cycle. The evolution of Bragg reflections of $\text{NaNi}_{0.5}\text{Ti}_{0.5}\text{O}_2$, along with the voltage profile, is given in Figure 3. After a continuous shift of the initial O_3 phase reflections, the appearance of new reflections can be clearly seen at the voltage corresponding to the beginning of the steep region in the charging curve. These reflections can be assigned to a sodium-deficient P_3 structure. A diffraction pattern and structural information about the P_3 phase are presented in Figure S1 and Table S1, respectively. After a short coexistence of both phases, the O_3 structure vanishes and the P_3 lattice undergoes a solid solution regime during further charge and subsequent discharge until O_3 reappears at the end of discharge.

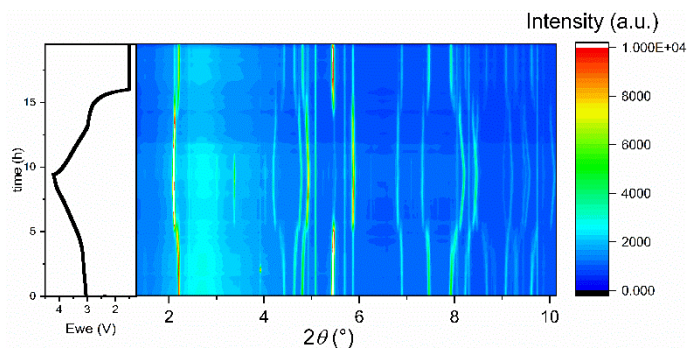


Figure 3. Contour plot of *operando* synchrotron XRD data ($\lambda = 0.20737(1) \text{ \AA}$) with the corresponding galvanostatic cycling curve. After five hours of charging, the appearance of a new structure is visible, which mostly transforms back into the original structure after twelve hours of discharging. For clarity, a plot of stacked diffraction patterns is presented in Figure S1c.

The lattice parameters of both phases obtained from these data, shown in Figure 4, allow a more detailed description of the non-trivial structural changes. The solid solution mechanism of the pristine O_3 phase reaches from its initial

sodium content of $x=1$ to $x=0.85$. Upon further desodiation, the P_3 structure appears, but it retains its composition since its lattice parameters remain constant while further sodium is removed from O_3 , producing a unit cell shrinkage in a -direction and an expansion in c -direction. Only after the remaining O_3 proportion vanishes at $x=0.65$, the P_3 phase starts to release sodium and undergoes a lattice shrinkage and expansion in the a - and c -directions, respectively. Note that the difference in the lattice parameters a , which reflects the bond length between transition metal and oxygen, is quite big for O_3 and P_3 phases, meaning existence of Ni in different valence states in both materials. Two scenarios, either coexistence of Ni^{3+} and Ni^{2+} , or Ni^{4+} and Ni^{2+} , are possible.

During the subsequent discharge, the P_3 phase exhibits the reversed changes until the O_3 form reappears at $x=0.65$. From this state of discharge, the composition of the P_3 phase does not change anymore, only its amount in the material. Afterwards, the fraction of O_3 increases, as well as its sodium content. At the end of discharge however, an amount of P_3 material (about 20 %) remains. This finding will be revived in later sections.

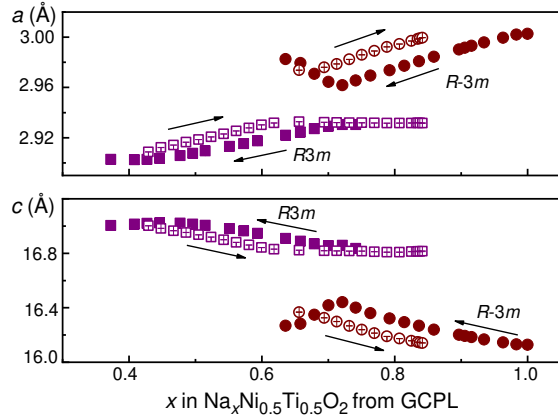


Figure 4. Lattice parameters of the pristine O_3 phase (brown circles) and the rising P_3 phase (magenta squares) during initial charge (full symbols) and discharge (hollow symbols). During charge, a decreases and c increases for both phases. Discharging reverses these changes.

Refinement of oxygen coordinates in both phases allowed analysis of interatomic distances between (Ni,Ti) and O, as presented in Figure 5. The starting M-O distance matches excellently with the theoretical value of 2.048 Å (considering the average of 50 % Ni^{2+} and 50 % Ti^{4+} coordinated octahedrally with O^{2-}).¹⁷ As sodium is extracted and nickel gets oxidized, the Ni-O bond shortens. At the desodiation cutoff, a distance of 1.93 Å is obtained, which points at possible mixtures of Ti^{4+} with Ni^{3+} and Ni^{4+} . The observed changes are reversible, except for a small hysteresis of M-O distances in the reappearing O_3 phase.

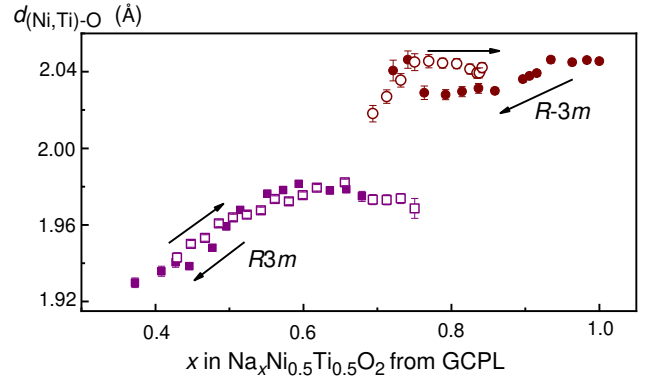


Figure 5. Average transition metal-oxygen distances in the O_3 (brown circles) and P_3 (magenta squares) phases. A decreasing trend for the charge process (full symbols) and an increase during discharge (hollow symbols) is observed, correlating with the a parameter.

As mentioned above, a fraction of the P_3 phase remains after discharging. The evolution of this phase content, calculated from Rietveld analysis, is presented in Figure 6. After galvanostatic discharging to 1.5 V, approximately 20 w/w % of the P_3 phase remain in the electrode. This content decreases only slowly to about 10 w/w-% after three hours of hold time at the sodiation cutoff potential.

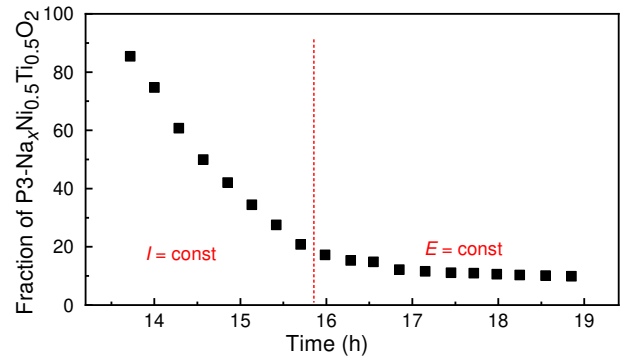


Figure 6. Calculated fraction of P_3 phase during discharge and hold period. At the end of the galvanostatic discharge, approximately 20 % of the P_3 structure remain. This fraction decreases only slowly during the potentiostatic period.

The quality of synchrotron diffraction data allowed to refine sodium site occupancies as a verification of the sodium content which is calculated from the current flow in the galvanostatic experiment. Both of these x values are opposed to each other in Figure 7. Ideally, the end points (the pure O_3 phase and the pure P_3 phase) should coincide with the dashed bisector line. While for the O_3 phase, sodium contents from GCPL and from Rietveld refinement are in reasonable accordance, a remarkable mismatch is seen for P_3 . In the charged state, 0.37 Na per formula unit should be present according to the electrochemical experiment, while the Rietveld analysis yields only 0.19 Na remaining in

the P3 phase. In order to explain this, multiple aspects have to be considered. Note, in additional experiments during monitoring the open-circuit voltage of i) Na metal and ii) $\text{NaNi}_{0.5}\text{Ti}_{0.5}\text{O}_2$ vs. Na in carbonate-based NaClO_4 -electrolytes we detected persistent fluctuations, representing a non-stable situation, see Figure S2. Recently, the instability of solid electrolyte interphases (SEI) in sodium batteries was attributed to a continuous dissolution of its major parts, giving rise to self-discharge phenomena.¹⁸ The observed mismatch of sodium contents provides further evidence for these explanations. Interestingly, the high-voltage region above 4 V has already been associated with side reactions of different origins, as for example for $\text{Na}_x\text{Ni}_{0.3}\text{Mn}_{0.7}\text{O}_2$ and $\text{Na}_x\text{Co}_{0.5}\text{Ti}_{0.5}\text{O}_2$.^{12,19} Therein, a stagnation of lattice parameters and a higher degree of desodiation according to GCPL compared to the refined occupancies were measured. In our case, the lattice parameters keep changing and GCPL delivers a lower desodiation state than the refined occupancies, pointing at a considerably different situation. Note that Rietveld refinement provides Na occupancy values for the crystalline phase only and the presence of amorphous domains containing Na cannot be determined. Another possibility for the discrepancy may be a partial delocalization of Na from its crystallographic site in the P3 phase and the random distribution in the interlayer space, giving rise to enhanced ionic transport.^{20,21}

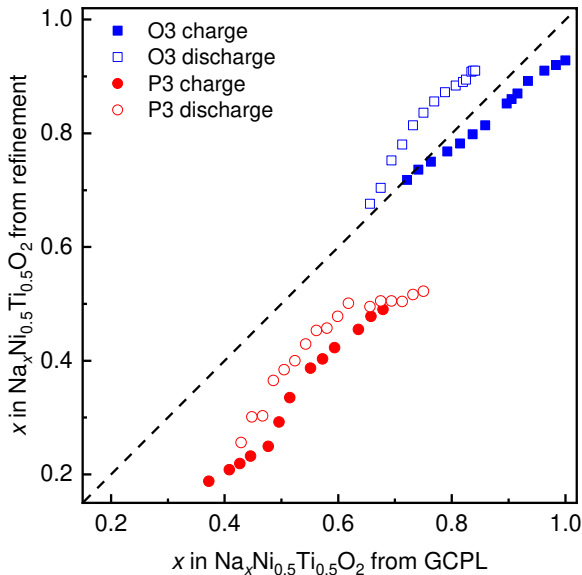


Figure 7. Comparison of sodium contents obtained from GCPL measurement and from Rietveld refinement.

Operando Evaluation of Reaction Mechanism (II): Local structure and valence state. Since two transition metals are present in the title compound, their individual role in the redox processes has to be examined carefully in order to understand the reaction mechanisms. Therefore, *operando* X-Ray absorption was performed at the Ni-K and Ti-K edges, respectively. Figure 8a depicts the evolution of Ni-K edge spectra during the first cycle. The valence state of the 3d transition metals is directly correlated with the

position of the absorption edge E , defined at $\mu = 0.8$.^{22,23} In the pristine state, the position of the absorption edge of the sample concurs well with the NiO reference, evidencing the Ni^{2+} state. Upon charging, the spectra shift towards higher energies, indicating the oxidation of Ni. The subsequent discharge causes an edge shift back to lower energies and therefore indicates the reduction of Ni. A plot of the edge positions at 80 % of the averaged post-edge intensity is given in Figure 8b. An almost linear trend in edge shifts is observed, yielding a total shift of ~ 2.5 eV, which is also reflected by the pre-edge peak position (Figure 8a inset). In the literature, varying relations between oxidation states and edge shifts are reported for Ni oxides, e.g. a shift of 1 eV²⁴ or 1.5 eV²⁵ per unit change in valency.

A linear fit of our data along with a Ni foil and NiO as standards reveals a shift of 2 eV per unit change of the Ni oxidation state, see Figure S3.

On the contrary, the Ti-K edge does not exhibit a measurable shift within the whole electrochemical process, as shown in Figure 9. This indicates complete redox inactivity of Ti in the potential window 1.5 V - 4.2 V vs. Na^+/Na , acting as a structure stabilizer only.

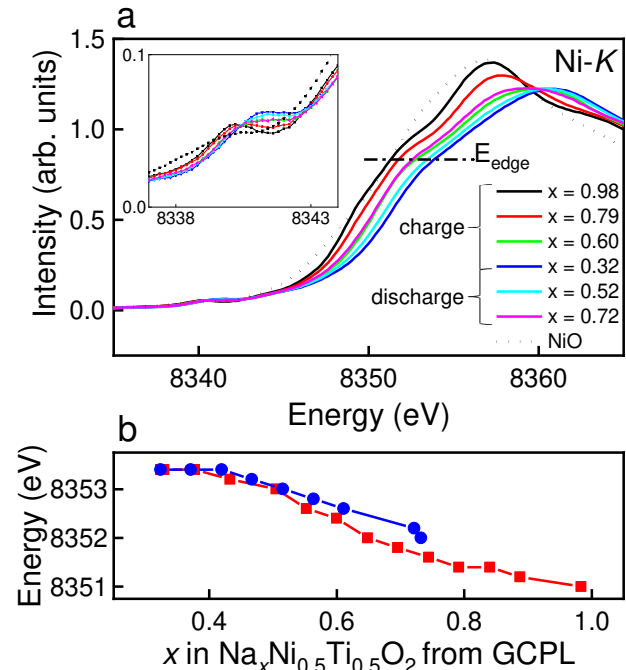


Figure 8. a) X-Ray absorption near edge structure at the Ni-K edge during charge and discharge. Inset: enlarged pre-edge peak. b) Edge shift of the Ni-K edge upon electrochemical cycling. Red squares indicate the charge half cycle, blue circles depict the discharge process.

The data quality allowed for fits of the extended X-ray absorption fine structure with the aim to determine the local environment of Ni ions (bond lengths Ni-O as the first coordination shell and Ni-(Ni,Ti) as second shell). The evolution of forward Fourier transformed spectra and an example spectrum, demonstrating the excellent fit quality,

are provided in Figure S4. Figure 10 provides the interatomic distances obtained from these fits. Ni-O distances, starting from 2.1 Å, are reversibly decreasing to 1.9 Å during charge while Ni-(Ni,Ti) distances change less severe from 2.95 Å to 2.90 Å. Therefore, in the pristine material Ti slightly contracts the crystal structure because the average Ni,Ti-O distance evaluated from Rietveld analysis is slightly shorter than the Ni-O distance (see Figure 5). In contrast, in the charged state it expands the lattice in comparison to the hypothetical “ Na_xNiO_2 ” structure. Detailed fit parameters are listed in Table S2.

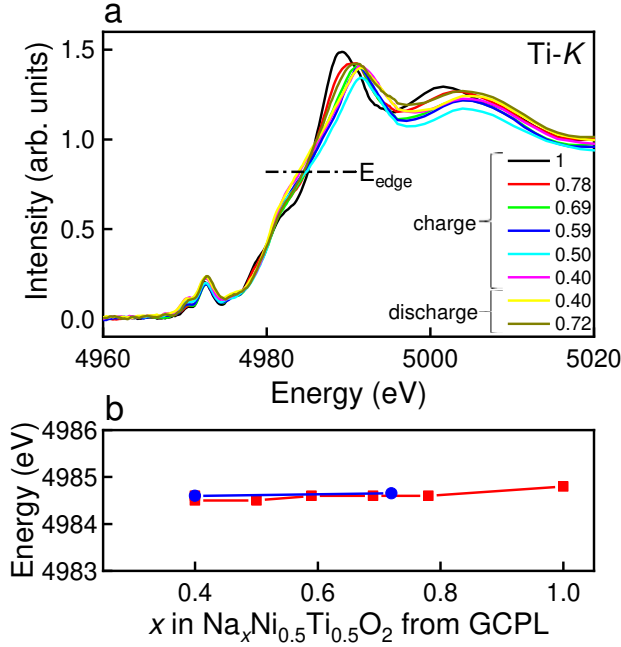


Figure 9. a) X-Ray absorption near edge structure of the Ti-K edge during the first cycle. b) Edge shift of the Ti-K edge upon electrochemical cycling. Red squares indicate the charge half cycle, blue circles depict the discharge process.

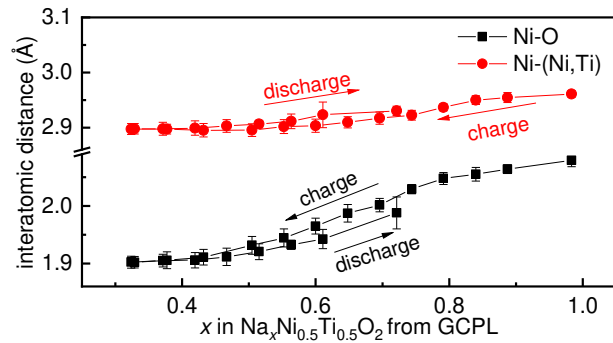


Figure 10. Nickel-oxygen and nickel-transition metal (Ni, Ti) distances, calculated from EXAFS. Both Ni-O as well as Ni-(Ni,Ti) decrease upon charge and reversibly increase again when the cell is discharged.

Magnetization Measurements. For further insights into transition metal valence states of $\text{Na}_x\text{Ni}_{0.5}\text{Ti}_{0.5}\text{O}_2$, *ex situ* magnetization measurements were carried out. All samples feature a paramagnetic behaviour above 130 K. Figure 11 clearly shows a lower paramagnetic moment for the charged state (P_3 phase), as compared to the pristine and the cycled material. The initially present Ni^{2+} (d^8 , $S=1$) is oxidized to either Ni^{3+} (d^7 , $S=1/2$, low-spin state) or directly to Ni^{4+} (d^6 , $S=0$, low-spin state) when the cell is charged. As both pathways are possible, and we cannot reliably distinguish between them, the charged state consists either of a $\text{Ni}^{3+}/\text{Ni}^{4+}$ or a $\text{Ni}^{2+}/\text{Ni}^{4+}$ mixture. The observed paramagnetic moments along with theoretical values are provided in Table 1. The magnetization curve after the first cycle almost replicates the curve of the pristine material, indicating the reversed reduction to Ni^{2+} . However, the slightly smaller paramagnetic moment gives further evidence of an incomplete back-transformation and a remaining P_3 fraction. Inverse magnetic susceptibilities of the measured data and the Curie-Weiss fits are shown in Figure S5.

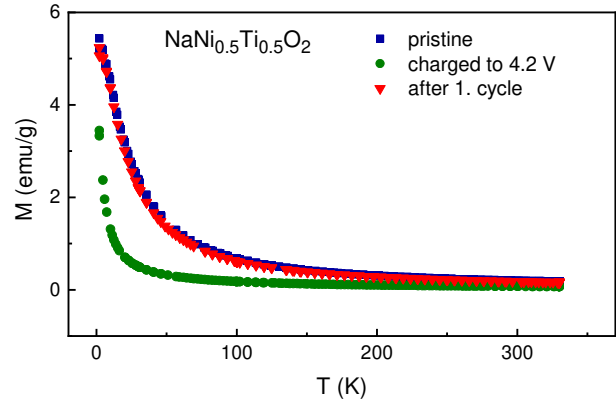


Figure 11. Magnetization measurements of $\text{Na}_x\text{Ni}_{0.5}\text{Ti}_{0.5}\text{O}_2$, performed at 6 T. The almost identity of pristine and cycled state indicate reversible behaviour, while a lower paramagnetic moment exists after charging.

Table 1. *Ex situ* Magnetization data.

Material	$\mu_{\text{eff}}(\text{exp})$, $\mu_{\text{B}}/\text{f.u.}$	θ , K	χ_0 , emu/mol	T range for fit, K	$\mu_{\text{eff}}(\text{theor})$, $\mu_{\text{B}}/\text{f.u.}$
$\text{O}_3\text{-NaNi}_{0.5}\text{Ti}_{0.5}\text{O}_2$	2.20(2)	18.5(4)	$-1.2(7) \times 10^{-5}$	130 - 330	2.0 for 0.5Ni^{2+} (d^8 , $S=1$)
$\text{P}_3\text{-Na}_{0.3}\text{Ni}_{0.5}\text{Ti}_{0.5}\text{O}_2$	1.10(2)	-3(1)	$1.87(6) \times 10^{-4}$	130 - 330	0.95 for 0.3Ni^{3+} (d^7 , $S=1/2$) and 0.2Ni^{4+} (d^6 , $S=0$), or 1.09 for 0.15Ni^{2+} (d^8 , $S=1$) and 0.35Ni^{4+} (d^6 , $S=0$)
" O_3 + P_3 "- $\text{Na}_{0.9}\text{Ni}_{0.5}\text{Ti}_{0.5}\text{O}_2$	2.05(2)	22(1)	$-1.7(2) \times 10^{-6}$	130 - 330	1.87 for 0.4Ni^{2+} (d^8 , $S=1$) and 0.1Ni^{3+} (d^7 , $S=1/2$), or 1.90 for 0.45Ni^{2+} (d^8 , $S=1$) and 0.05Ni^{4+} (d^6 , $S=0$)

DISCUSSION

Since layered sodium oxides are liable to show significant structural changes during (de-)sodiation, they remain a black box until substantiated conclusions are drawn from *operando* studies.

An obvious advantage of Ti doping is its superior structural stabilization of the layered oxide in comparison to undoped materials or materials with different transition metal substitution. Undoped NaNiO_2 exhibits a couple of transformations upon desodiation/sodiation,²⁶ which are not reversible below 3.0 V and over 4.0 V. Substitution of 50% Ni by Ti allows to significantly change the reaction mechanism resulting in the only transformation being $\text{O}_3 \rightarrow \text{P}_3 \rightarrow \text{O}_3$, as we showed by *operando* XRD measurements. Note that there is an exciting similarity in the reaction mechanism of Ti-substituted layered materials as our recent work on $\text{NaCo}_{0.5}\text{Ti}_{0.5}\text{O}_2$ revealed:¹⁹ the $\text{O}_3 \rightarrow \text{P}_3 \rightarrow \text{O}_3$ transformation is also the only reaction observed in case of the Co-containing compound upon Na-removal and insertion. In both systems, Ti does not participate in the redox process, as shown by *operando* XAS studies. In case of $\text{Na}_x\text{Co}_{0.5}\text{Ti}_{0.5}\text{O}_2$, a complex interplay of charge and spin transfer of Co results in a large volume change of more than 5 Å³ per unit cell during the $\text{O}_3 \rightarrow \text{P}_3$ transformation, producing a large potential hysteresis between charge and discharge which in turn dramatically reduces the energy density.¹⁹ The volume change between P_3 and O_3 modifications of $\text{Na}_x\text{Ni}_{0.5}\text{Ti}_{0.5}\text{O}_2$ is less than 1 Å³, explaining the absence of a voltage hysteresis.

For $\text{O}_3\text{-Na}_x\text{Ni}_{0.5}\text{Mn}_{0.5}\text{O}_2$, four structural transformations occur during sodium extraction,⁴ while the isostructural Ti-containing material shows only one. We conclude that the buffering effect of Ti^{4+} cations is therefore stronger than the one of Mn^{4+} . While Ti^{4+} (0.605 Å) is only slightly smaller than Ni^{2+} (0.69 Å), the difference between Mn^{4+} (0.53 Å) and Ni^{2+} is much bigger. The introduction of Ti^{4+} causes a slight lattice contraction, leading to stabilization

whereas the introduction of Mn^{4+} causes a much stronger contracting force, resulting in less stabilization as the lattice is "over-contracted". Therefore, the presence of Mn^{4+} is more likely to lead to phase transformations as the sodiation state changes. The electrochemical performance of both oxides is comparable and Mn as well as Ti are electrochemically inactive. The C-rate dependence that has been observed for the two O_3 structures indicates a generally hampered Na diffusion, which is in accordance with the literature, where superior kinetics in P_2 phases have often been reported.^{29,30} The main difference between the P_2 and P_3 phases is the stacking sequence of oxygen layers yielding the number of sheets within a unit cell (AABB... vs. AABBCC...). Guo et al. compared $\text{P}_2\text{-Na}_{0.62}\text{Ti}_{0.37}\text{Cr}_{0.63}\text{O}_2$ to $\text{P}_3\text{-Na}_{0.63}\text{Ti}_{0.37}\text{Cr}_{0.63}\text{O}_2$ in terms of structural and electrochemical properties as well as their sodium migration characteristics.³⁰ The superior capacity retention and rate capability of the P_2 phase were attributed to lower sodium diffusion barriers, which was predicted by DFT calculations and validated experimentally by GITT measurements. On the other hand, P_2 structures, usually containing ~0.67 Na per formula unit, limit the electrochemical capacity from the beginning as less sodium can be extracted.

As mentioned, $\text{Na}_x\text{Ni}_{0.5}\text{Ti}_{0.5}\text{O}_2$ still shows capacity loss upon cycling, especially when increasing the current density from 0.2C to 1C.³ The capacity loss is much more pronounced for the related Li-containing $\text{Li}_x\text{Ni}_{0.45}\text{Ti}_{0.55}\text{O}_2$ in Li-ion batteries.²⁷ This was explained by Ti^{4+} migration into the Li layers during charge, which impedes further Li diffusion. Also, intermixing of Li and Ni is well known, as for LiNiO_2 .²⁸ This effect is neglectable for $\text{Na}_x\text{Ni}_{0.5}\text{Ti}_{0.5}\text{O}_2$ since Na shows a largely different radius compared to Ni and Ti (1.02 Å vs. 0.69 Å for Ni^{2+} and 0.605 Å for Ti^{4+} in oxygen octahedra, respectively) and is highly unlikely to be the reason for the observed capacity fading.

However, the $\text{O}_3 \rightarrow \text{P}_3 \rightarrow \text{O}_3$ transformation in $\text{Na}_x\text{Ni}_{0.5}\text{Ti}_{0.5}\text{O}_2$ repeated over many charge-discharge cycles

can lead to accumulation of structural defects which act as fault centres hindering Na diffusion. We can indirectly confirm this by XRD measurements of the material after long-term cycling (see Figure S6): relatively low intensities and shape anomalies in Bragg reflections suggest a lot of structural defects and even partial amorphization of the material. If we provide the system with more time for completing the transformation by implementing constant voltage regimes during cycling, we can improve capacity values for subsequent cycles. However, this improvement disappears during further cycling, see Figure S7. Therefore, further detailed studies are needed to understand the Na-diffusion mechanisms in dependence on the doping elements and resulting structure, unit cell dimensions and changes.

Our findings together with the literature reports demonstrate once more the attractiveness of Ni-containing layered oxides as electrode materials for sodium-ion batteries because of their high redox potential as well as reduced cost and toxicity in comparison to Co. However, they still need to be optimized in terms of the material composition and morphologies. Compared to their lithium analogues, these materials are still much less understood and, although beneficial electrochemical properties have been demonstrated multiple times, much effort still has to be spent in order to advance in understanding this family of compounds.

CONCLUSIONS

O₃-type layered NaNi_{0.5}Ti_{0.5}O₂ has been synthesized and comprehensively characterized in sodium-ion batteries. A combination of *operando* techniques was applied for a deep understanding of the cathode material. Synchrotron diffraction revealed a reversible transformation into a P₃ layered structure during desodiation. The corresponding back-transformation remains incomplete and a P₃ fraction is still present after subsequently sodiating the material. Compared to NaNiO₂ and NaNi_{0.5}Mn_{0.5}O₂, the series of structural changes is dramatically reduced due to the stabilizing effect of Ti⁴⁺ within the structure. Additionally, the average potential is increased compared to half cells using NaNiO₂ cathodes. X-Ray absorption studies revealed the electrochemical inactivity of Ti⁴⁺ under the investigated conditions in the entire potential range. The redox process is sustained by a reversible oxidation and reduction of the initially present Ni²⁺, as further evidenced by magnetization measurements. Similar to other layered O₃ sodium oxides this material shows a strong dependence on C-rate,³ demonstrating the high importance of diffusion ways for sodium cations within the interlayers between transition metal and oxygen planes. Our findings demonstrate the urgent need of profound studies on future energy storage compounds since only thorough understanding will allow their design and the development of advanced handling procedures.

ASSOCIATED CONTENT

Supporting Information. Structural parameters of O₃ and P₃ phases, OCV evolution, XAS edge shifts, Forward Fourier Transformed XAS spectra, EXAFS fit parameters, inverse susceptibility plots, XRD in cycled state and cycling performance. This material is available free of charge via the Internet at <http://pubs.acs.org>.

AUTHOR INFORMATION

Corresponding Author

* E-mail: s.maletti@ifw-dresden.de

* E-mail: d.mikhailova@ifw-dresden.de

ORCID

Sebastian Maletti: 0000-0001-5308-658X

Daria Mikhailova: 0000-0002-8197-1807

Alexander Schökel: 0000-0002-3680-8648

Author Contributions

The manuscript was written with contributions from all authors. All authors have given approval to the final version of the manuscript.

ACKNOWLEDGMENT

This research has benefitted from beamtime allocation at beamlines Po2.1 and P65 at the PETRA III synchrotron (DESY, Hamburg, Germany). The authors are deeply grateful for practical help provided by Haneen Albukai, Ronny Buckan (both IFW Dresden), Dr. Edmund Welter and Dr. Martin Etter (both DESY). The work in Dresden was supported by the European Union and the Free State of Saxony under the TTKin project (SAB grant no. 100225299).

REFERENCES

- (1) Vassilaras, P.; Ma, X.; Chen, H.; Ceder, G. Electrochemical Properties of Monoclinic NaNiO₂. *J. Electrochem. Soc.* **2013**, 160, A207–A211.
- (2) Han, M. H.; Gonzalo, E.; Casas-Cabanas, M.; Rojo, T. Structural Evolution and Electrochemistry of Monoclinic NaNiO₂ upon the First Cycling Process. *J. Power Sources* **2014**, 258, 266–271.
- (3) Yu, H.; Guo, S.; Zhu, Y.; Ishida, M.; Zhou, H. Novel Titanium-based O₃-type NaTi_{0.5}Ni_{0.5}O₂ as a Cathode Material for Sodium-Ion Batteries. *Chem. Commun. (Camb)*. **2014**, 50, 457–459.
- (4) Komaba, S.; Naoaki, Y.; Nakayama, T.; Ogata, A.; Ishikawa, T.; Nakai, I. Study on the Reversible Electrode Reaction of Na_{1-x}Ni_{0.5}Mn_{0.5}O₂ for a Rechargeable Sodium-Ion Battery. *Inorg. Chem.* **2012**, 51, 6211–6220.
- (5) Wang, P.-F.; Yao, H.-R.; Liu, X.-Y.; Zhang, J.-N.; Gu, L.; Yu, X.-Q.; Yin, Y.-X.; Guo, Y.-G. Ti-Substituted NaNi_{0.5}Mn_{0.5-x}Ti_xO₂ Cathodes with Reversible O₃-P₃ Phase Transition for High-Performance Sodium-Ion Batteries. *Adv. Mater.* **2017**, 29, 1–7.
- (6) Guo, S.; Yu, H.; Liu, P.; Ren, Y.; Zhang, T.; Chen, M.; Ishida, M.; Zhu, H. High-Performance Symmetric Sodium-Ion Batteries Using a New, Bipolar O₃-type Material, Na_{0.8}Ni_{0.4}Ti_{0.6}O₂. *Energy Environ. Sci.* **2015**, 8, 1237–1244.

- (7) Shanmugam, R.; Lai, W. $\text{Na}_{2/3}\text{Ni}_{1/3}\text{Ti}_{2/3}\text{O}_2$: “Bi-Functional” Electrode Materials for Na-Ion Batteries. *ECs Electrochem. Lett.* **2014**, 3, A23–A25.
- (8) Fielden, R.; Obrovac, M. N. Low Voltage Sodium Intercalation in $\text{Na}_x\text{Ni}_{x/2}\text{Ti}_{1-x/2}\text{O}_2$ ($0.5 \leq x \leq 1.0$). *J. Electrochem. Soc.* **2014**, 161, A1158–A1163.
- (9) Chen, Q.; Lai, W. A Computational Study on P2-type $\text{Na}_x[\text{Ni}_{1/3}\text{Ti}_{2/3}]\text{O}_2$ as Bi-Functional Electrode Materials for Na-Ion Batteries. *J. Electrochem. Soc.* **2018**, 165, A3586–A3594.
- (10) Mariyappan, S.; Wang, Q.; Tarascon, J. M. Will Sodium Layered Oxides Ever Be Competitive for Sodium Ion Battery Applications? *J. Electrochem. Soc.* **2018**, 165, A3714–A3722.
- (11) Wang, H.; Xiao, Y.; Sun, C.; Lai, C.; Ai, X. A Type of Sodium-Ion Full Cell with a Layered $\text{NaNi}_{0.5}\text{Ti}_{0.5}\text{O}_2$ Cathode and a Pre-Sodiated Hard Carbon Anode. *RSC Adv.* **2015**, 5, 106519–106522.
- (12) Kjeldgaard, S.; Birgisson, S.; Kielland, A. G.; Iversen, B. B. *Operando* Powder X-Ray Diffraction Study of P2- $\text{Na}_x\text{Ni}_{0.3}\text{Mn}_{0.7}\text{O}_2$ Cathode Material During Electrochemical Cycling. *J. Appl. Crystallogr.* **2018**, 51, 1304–1310.
- (13) Birgisson, S.; Shen, Y.; Iversen, B. B. *In Operando* Observation of Sodium Ion Diffusion in a Layered Sodium Transition Metal Oxide Cathode Material, P2 $\text{Na}_x\text{Co}_{0.7}\text{Mn}_{0.3}\text{O}_2$. *Chem. Commun.* **2017**, 53, 1160–1163.
- (14) Herklotz, M.; Weiß, J.; Ahrens, E.; Yavuz, M.; Mereacre, L.; Kiziltas-Yavuz, N.; Dräger, C.; Ehrenberg, H.; Eckert, J.; Fauth, F.; Giebeler, L.; Knapp, M. A Novel High-Throughput Setup for *In Situ* Powder Diffraction on Coin Cell Batteries. *J. Appl. Crystallogr.* **2016**, 49, 340–345.
- (15) Roisnel, T.; Rodriguez-Carvajal, J. WinPLOTR: a Windows Tool for Powder Diffraction Pattern Analysis. *Mater. Sci. Forum* **2001**, 378–381.
- (16) Rehr, J. J.; de Mustre Leon, J.; Zabinsky, S. I.; Albers, R. C. Theoretical X-Ray Absorption Fine Structure Standards. *J. Am. Chem. Soc.* **1991**, 113, 5135–5140.
- (17) Shannon, R. D. Revised Effective Ionic Radii and Systematic Studies of Interatomic Distances in Halides and Chalcogenides. *Acta Crystallogr. Sect. A* **1976**, 32, 751–767.
- (18) Mogensen, R.; Brandell, D.; Younesi, R. Solubility of the Solid Electrolyte Interphase (SEI) in Sodium Ion Batteries. *ACS Energy Lett.* **2016**, 1, 1173–1178.
- (19) Maletti, S.; Giebeler, L.; Oswald, S.; Tsirlin, A. A.; Senyshyn, A.; Michaelis, A.; Mikhailova, D. Irreversible Made Reversible: Increasing the Electrochemical Capacity by Understanding the Structural Transformations of $\text{Na}_x\text{Co}_{0.5}\text{Ti}_{0.5}\text{O}_2$. *ACS Appl. Mater. Interfaces* **2018**, 10, 36108–36119.
- (20) Cherkaoui, F.; Viala, J. C.; Delmas, C.; Hagenmuller, P. Crystal Chemistry and Ionic Conductivity of a New Nasicon-Related Solid Solution $\text{Na}_{1+x}\text{Zr}_{2-x}\text{Mg}_{x/2}(\text{PO}_4)_3$. *Solid State Ionics* **1986**, 21, 333–337.
- (21) Cherkaoui, F.; Villeneuve, G.; Hagenmuller, P.; Delmas, C. Sodium Motion in the Nasicon Related $\text{Na}_{1+x}\text{Zr}_{2-x}\text{In}_x(\text{PO}_4)_3$ Solid Solution: An NMR Study. *J. Solid State Chem.* **1986**, 65, 293–300.
- (22) Poltavets, V. V.; Croft, M.; Greenblatt, M. Charge Transfer, Hybridization and Local Inhomogeneity Effects in $\text{Na}_x\text{CoO}_2 \cdot y\text{H}_2\text{O}$: An X-Ray Absorption Spectroscopy Study. *Phys. Rev. B - Condens. Matter Mater. Phys.* **2006**, 74, 1–8.
- (23) Saitoh, T.; Mizokawa, T.; Abbate, M.; Takeda, Y.; Takano, M.; Fujimori, A. Electronic Structure and Magnetic States in $\text{La}_{1-x}\text{Sr}_x\text{CoO}_3$ Studied by Photoemission and X-Ray-Absorption Spectroscopy. *Phys. Rev. B*, **2002**, 56, 1290–1295.
- (24) Mansour, A. N.; Melendres, C. A.; Pankuch, M.; Brizzolara, R. A. X-ray Absorption Fine Structure Spectra and the Oxidation State of Nickel in Some of its Oxycompounds. *J. Electrochem. Soc.* **1994**, 141, L69–L71.
- (25) O’Grady, W. E.; Pandya, K. I.; Swider, K. E.; Corrigan, D. A. In Situ X-Ray Absorption Near-Edge Structure Evidence for Quadrivalent Nickel in Nickel Battery Electrodes. *J. Electrochem. Soc.* **1996**, 143, 1613–1616.
- (26) Wang, L.; Wang, J.; Zhang, X.; Ren, Y.; Zuo, P.; Yin, G.; Wang, J. Unravelling the Origin of Irreversible Capacity Loss in NaNiO_2 for High Voltage Sodium Ion Batteries. *Nano Energy* **2017**, 34, 215–223.
- (27) Kang, K.; Carlier, D.; Reed, J.; Arroyo, E. M.; Ceder, G.; Croguennec, L.; Delmas, C. Synthesis and Electrochemical Properties of Layered $\text{Li}_{0.9}\text{Ni}_{0.45}\text{Ti}_{0.55}\text{O}_2$. *Chem. Mater.* **2003**, 15, 4503–4507.
- (28) Julien, C.; Mauger, A.; Vijh, A.; Zaghib, K. Lithium Batteries. Science and Technology. *Springer* **2015**.
- (29) Kubota, K.; Kumakura, S.; Yoda, Y.; Kuroki, K.; Komaba, S. Electrochemistry and Solid-State Chemistry of NaMeO_2 (Me = 3d Transition Metals). *Adv. Energy Mater.* **2018**, 8, 1–30.
- (30) Guo, S.; Sun, Y.; Yi, J.; Zhu, K.; Liu, P.; Zhu, Y.; Zhu, G.; Chen, M.; Ishida, M.; Zhou, H. Understanding Sodium-Ion Diffusion in Layered P2 and P3 Oxides Via Experiments and First-Principles Calculations: a Bridge Between Crystal Structure and Electrochemical Performance. *NPG Asia Mater.* **2016**, 8, e266.

Table of Contents Graphic

